Rosendo López, María; Peñaranda, Fernando; Christensen, Johan; San José, Pablo. (2020). Flat Bands in Magic-Angle Vibrating. *Physical Review Letters*, 125(21), 214301, pp. 1-6.

DOI: https://doi.org/10.1103/PhysRevLett.125.214301

# Flat Bands in Magic-Angle Vibrating Plates

María Rosendo López,[1] Fernando Peñaranda,[2] Johan Christensen,[1] and Pablo San-Jose[2,*]
[1]Department of Physics, Universidad Carlos III de Madrid, ES-28916 Leganés, Madrid, Spain
[2]Instituto de Ciencia de Materiales de Madrid, Consejo Superior de Investigaciones Científicas (ICMM-CSIC), ES-28049 Madrid, Spain

(Received 27 August 2020; accepted 8 October 2020; published 20 November 2020)

Twisted bilayer graphene develops quasiflat bands at specific "magic" interlayer rotation angles through an unconventional mechanism connected to carrier chirality. Quasiflat bands are responsible for a wealth of exotic, correlated-electron phases in the system. In this Letter, we propose a mechanical analog of twisted bilayer graphene made of two vibrating plates patterned with a honeycomb mesh of masses and coupled across a continuum elastic medium. We show that flexural waves in the device exhibit vanishing group velocity and quasiflat bands at magic angles in close correspondence with electrons in graphene models. The strong similarities of spectral structure and spatial eigenmodes in the two systems demonstrate the chiral nature of the mechanical flat bands. We derive analytical expressions that quantitatively connect the mechanical and electronic models, which allow us to predict the parameters required for an experimental realization of our proposal.

DOI: 10.1103/PhysRevLett.125.214301

Classical analogs of quantum electronic systems in acoustic and mechanical settings offer a new and exciting perspective on nontrivial electronic phenomena such as topological insulating phases, topologically protected edge states, Weyl and Dirac semimetallic phases, or Majorana bound states [1–9]. An important appeal of these classical analogs is their easy fabrication and tunability, typically much simpler than for their electronic counterparts. They often reveal new and unexpected effects in a classical context and deep connections between very different physical systems [10].

A remarkable electronic effect that has to date received little attention in the acoustic and mechanical context is flat-band formation in twisted bilayer graphene (TBG). TBG is composed of two graphene monolayers placed in direct contact with each other after rotating one of them by a certain angle $\theta$ [11–14]. Each monolayer on its own possesses a massless Dirac spectrum with a certain group velocity $v_0$ around Dirac wave vectors $\pm\boldsymbol{K}$ [15,16]. The crystalline moiré pattern produced by the interlayer rotation, Fig. 1(a), was shown [11,17] to produce a $\theta$-dependent suppression of the velocity $v(\theta)$, even reaching $v(\theta_i) = 0$ at a series of so-called magic angles $\theta_{i=1,2,\ldots}$ [12,13,18,19]. At these twist angles, the TBG Dirac cones collapse into quasiflat bands at the half-filling Fermi energy. The mechanism behind flat-band formation in the system is highly unconventional and is not the result of exponential wave-function localization (although algebraic localization at AA moiré region does takes place [20]) but of carrier chirality and effective non-Abelian gauge fields produced by the modulation of the interlayer coupling [21,22]. The development of chirality-driven quasiflat bands produces a rich phase diagram of correlated electronic phases triggered by many-body instabilities [23–28], which include Mott-insulating phases [29,30], nonconventional superconductivity (possibly related to that of cuprates) [30–33], strange-metal behavior [34,35], and two-dimensional magnetism [30,31,36–39]. These correlated phases are experimentally found to emerge at the first magic angle and are thus generally understood as a nontrivial consequence of quasiflat-band formation.

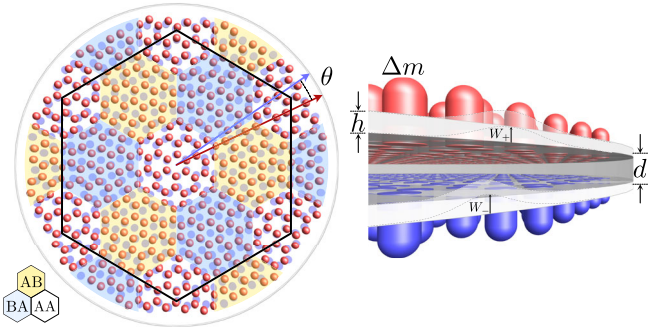


FIG. 1. Mechanical analog of twisted bilayer graphene: two vibrating plates of thickness $h$, density $\rho$, Young modulus $E$, and Poisson ratio $\nu$, patterned with a honeycomb lattice of $\Delta m$ masses (blue and red) and lattice constant $a$, and coupled across an elastic medium of thickness $d$ and Young modulus $E_d$. Upon changing the relative plate rotation angle $\theta$, a moiré pattern of alternating AA/AB/BA stacking alignments emerges, which modifies the group velocity of out-of-plane (flexural) modes ($W_\pm$). At specific ("magic") angles $\theta_i$, the group velocity vanishes, and quasiflat flexural bands develop. A possible realistic implementation could use $LiNbO_3$ plates and a rubber spacer, with $h \approx 1$ $\mu$m, $\rho \approx 4640$ kg/m$^3$, $E \approx 170$ GPa, $\nu \approx 0.25$, $\Delta m \approx 5.8$ ng, $a \approx 24$ $\mu$m, $d \approx 5$ $\mu$m, and $E_d \approx 10$ MPa. This yields the dimensionless parameters $\gamma \approx 2.5$, $\kappa \approx 30$, and $\Omega_D \approx 6.3$ (around 20 MHz) [see Eq. (4)] and a first magic angle at $\theta_1 \approx 1.6°$.

 

In this Letter, we propose a mechanical analog of TBG consisting of two elastic plates, supporting flexural (out-of-plane) vibrations. The plates are homogeneously coupled across a thin elastic medium, and a honeycomb pattern of pointlike masses is attached to each (see Fig. 1). We demonstrate a strong modulation of the flexural wave group velocity with the interplate rotation angle $\theta$, and the emergence of quasiflat flexural-mode bands at magic angles in close correspondence with the electronic counterpart. We showcase these effects by numerically solving the multiple-scattering problem of flexural modes on the attached masses as a function of $\theta$. The freezing of flexural vibrations into quasiflat bands happens at specific magic angles that in turn depend on mechanical parameters. We also derive approximate analytical expressions that connect the mechanical description of our system to the canonical electronic models used for TBG, establishing a precise connection between the two. The mapping allows us to directly compare the different spatial structure of eigenstates in equivalent mechanical and electronic systems. A realistic experimental implementation of our proposal is possible, with an example of fabrication parameters summarized in Fig. 1.

*Structured double plates.*—Consider flexural waves with amplitudes $W_l$ in two thin plates $l = \pm$ of uniform mass density $\rho$, thickness $h$, Young modulus $E$, Poisson ratio $\nu$, and bending stiffness $D = Eh^3/[12(1-\nu^2)]$. The vibrations of the two layers are elastically coupled locally by a linear intermediate medium of thickness $d$ and Young modulus $E_d$. We structure each plate with a honeycomb lattice of point masses represented by a mass density perturbation $\delta\rho_l(\boldsymbol{r})$ on plate $l$ (see sketch in Fig. 1). The equation of motion governing flexural waves of small amplitude $W \ll h$ in the system can be approximated by two coupled Germain–Lagrange equations. In the frequency $\omega$ domain, these read [40]

$$\sum_{l'}\left[\left(h\rho\omega^2 - D\nabla^4 - \frac{E_d}{d}\right)\tau_0^{ll'} + \frac{E_d}{d}\tau_x^{ll'}\right]W_{l'}(\boldsymbol{r},\omega) = -h\omega^2\delta\rho_l(\boldsymbol{r})W_l(\boldsymbol{r},\omega). \quad (1)$$

Here, the Pauli matrices $\tau_x$ and $\tau_0$ act on the "layer" (plate) index $l$. The rotation angle between layers enters the mass density perturbation $\delta\rho_l(\boldsymbol{r})$, which we write as

$$\delta\rho_l(\boldsymbol{r}) = \sum_{\alpha=A,B}\sum_{\boldsymbol{r}_\alpha^l}\frac{\Delta m}{A_c h}\delta(\boldsymbol{r}-\boldsymbol{r}_\alpha^l), \quad (2)$$

where $\boldsymbol{r}_{A,B}^l = n_1\boldsymbol{a}_1^l + n_2\boldsymbol{a}_2^l \mp (\boldsymbol{a}_1^l + \boldsymbol{a}_2^l)/6$ for integer $n_{1,2}$ denotes the positions of the point masses $\Delta m$ in layer $l = \pm$. The point masses form a honeycomb lattice with Bravais vectors $\boldsymbol{a}_{1,2}^l = a\mathcal{U}(l\theta/2)[\pm\cos(\pi/3), \sin(\pi/3)]$ on each layer $l$, with $\mathcal{U}(\theta)$ the relative rotation between layers and $a$ the honeycomb lattice period. $A_c = \sqrt{3}a^2/2$ stands for the area of the honeycomb unit cell. For our numerics, we restrict $\theta$ to commensurate rotations $\theta = \arccos[(3m^2+3m+1/2)/(3m^2+3m+1)]$ for some integer $m$. Under this constraint the moiré pattern resulting from overlapping the two plates is exactly periodic, with a period $L_m = a/[2\sin(\theta/2)]$.

To compare the double plate system to TBG, it is useful to recast Eq. (1) into a dimensionless form:

$$\sum_{l'}[(\Omega^2 - a^4\nabla^4 - \kappa)\tau_0^{ll'} + \kappa\tau_x^{ll'}]w_{l'}(\boldsymbol{r},\omega) = -\gamma\Omega^2\sum_{\alpha=A,B}\sum_{\boldsymbol{r}_\alpha^l}\delta(\boldsymbol{r}-\boldsymbol{r}_\alpha^l)w_l(\boldsymbol{r},\omega), \quad (3)$$

where we have introduced the dimensionless vibration amplitude $w = (D/a^4)W$ and dimensionless constants

$$\Omega^2 = \frac{a^4 h\rho\omega^2}{D} \qquad \kappa = \frac{a^4 E_d}{Dd} \qquad \gamma = \frac{\Delta m}{\rho h A_c} \quad (4)$$

Results.—Solving the eigenvalues $\Omega$ of Eq. (3) in wave vector $\boldsymbol{k}$ space in the large angle regime [41], we obtain the wave dispersions shown in Fig. 2. They are presented along a cut $\Gamma K_- M K_+ \Gamma$ of the moiré Brillouin zone for three distinct cases. The $\boldsymbol{K}_l$ Dirac wave vectors of the two layers are located at $\boldsymbol{K}_\pm = \mathcal{U}(\pm\theta/2)(4\pi/3a, 0)$. In (a) we show the solution for a single plate $l = -$. The dispersion clearly shows the emergence of a Dirac cone at $\boldsymbol{k} = \boldsymbol{K}_-$ (blue lines) around $\Omega = \Omega_D \approx 6$ when the mass lattice is added to the plate [1,2]. Panel (b) shows the spectrum for two decoupled plates ($\kappa = 0$) with a relative $\theta$ rotation. The Dirac cone of the second $l = +$ plate (red lines) appears at momentum $\boldsymbol{k} = \boldsymbol{K}_+$ and crosses the one from the $l = -$ plate at the $M$ point. Finally, panel (c) shows the spectrum for the two plates coupled by a finite plate coupling $\kappa$. An anticrossing between the two Dirac cone emerges, producing a van Hove singularity in the density of states of the system. This is exactly the phenomenology predicted [11] and observed [17] for TBG at not-so-small angles, $\theta \gtrsim 3°$. Note, however, that the formulation of the system model is very different from that of TBG. In contrast to the wave equation Eq. (3), TBG is usually described using the TBG continuum Hamiltonian [14], which can be succinctly written as [21]

$$H(\boldsymbol{k}) = \begin{pmatrix} t_0\Omega_D & \Pi_+^\dagger & V_{\mathrm{AA}}(\boldsymbol{r})^* & V_{\mathrm{BA}}(\boldsymbol{r})^* \\ \Pi_+ & t_0\Omega_D & V_{\mathrm{AB}}(\boldsymbol{r})^* & V_{\mathrm{AA}}(\boldsymbol{r})^* \\ V_{\mathrm{AA}}(\boldsymbol{r}) & V_{\mathrm{AB}}(\boldsymbol{r}) & t_0\Omega_D & \Pi_-^\dagger \\ V_{\mathrm{BA}}(\boldsymbol{r}) & V_{\mathrm{AA}}(\boldsymbol{r}) & \Pi_- & t_0\Omega_D \end{pmatrix}$$

$$\Pi_\pm = (k_x + ik_y \mp i\Delta K/2)v_0$$

$$\Delta K = |\boldsymbol{K}_+ - \boldsymbol{K}_-| = \frac{4\pi}{3a}2\sin\frac{\theta}{2} = \frac{4\pi}{3L_m}$$

$$V_\alpha = \frac{t_\perp}{3}[1 + e^{i\boldsymbol{G}_1(\boldsymbol{r}-\boldsymbol{r}_\alpha)} + e^{i\boldsymbol{G}_2(\boldsymbol{r}-\boldsymbol{r}_\alpha)}]$$

$$\boldsymbol{r}_{\mathrm{AA}}(\boldsymbol{r}) = 0, \qquad \boldsymbol{r}_{\mathrm{AB}} = -\boldsymbol{r}_{\mathrm{BA}} = \left(\frac{L_m}{\sqrt{3}}, 0\right). \quad (5)$$

The TBG band structure $\epsilon(\boldsymbol{k}) \equiv t_0\Omega(\boldsymbol{k})$ and the corresponding eigenstates $\psi(\boldsymbol{k})$ are obtained from the eigenvalue equation $H(\boldsymbol{k})\psi(\boldsymbol{k}) = \epsilon(\boldsymbol{k})\psi(\boldsymbol{k})$. The model exhibits the explicit $4 \times 4$ pseudospin-layer structure of a bilayer Dirac system, unlike the plate equation Eq. (3). The parameters specific to this model are the energy scale $t_0 \approx 2.7$ eV (intralayer hopping amplitude, or one third of the monolayer bandwidth), the twist angle $\theta$ or period $L_m$ [which enters through the moiré momenta $\boldsymbol{G}_{1,2} = (2\pi/L_m)[\pm(1/\sqrt{3}), 1]$], the Dirac velocity $v_0$ of the decoupled layers, the Fermi energy at half-filling $t_0\Omega_D$, and the interlayer hopping $t_\perp$ [whose moiré-induced modulation in the plane is captured by the $V_\alpha(\boldsymbol{r})$ functions]. $t_\perp$ plays a role analogous to $\kappa$ in the coupled plates, although in the latter the coupling is spatially uniform. The above TBG model neglects any particle-hole asymmetries in the decoupled layers around the Dirac point, which would arise in particular from finite next-nearest-neighbor hoppings in plane. It also assumes negligible layer strains and identical $V_\alpha$ coefficients. Both conditions are sometimes relaxed in more elaborate versions of the model.

We can formally connect the mechanical and electronic models analytically. The resulting mapping is valid to second order in the effective plate coupling $\kappa/|a\boldsymbol{K}|^4$. The starting point is a projection of the plane wave basis into a "tight-binding" basis of flexural modes spatially localized at the point masses on each layer. By carefully integrating out the remaining plate vibrations between scatterers in Eq. (3), the continuum TBG model of Eq. (5) emerges for frequencies close to the Dirac point and small couplings $\kappa$. The detailed derivation is presented in full in the Supplemental Material [41]. Here we present only the final result connecting the plate parameters in Eq. (4) to the equivalent TBG parameters in Eq. (5),

$$\Omega_D \approx \frac{a^2|\boldsymbol{K}|^2}{\sqrt{1+3\gamma}}\left(1+\frac{\kappa}{2|a\boldsymbol{K}|^4}\right) \tag{6}$$

$$v_0 \approx \frac{t_0}{\hbar}\frac{a^2|\boldsymbol{K}|}{\sqrt{1+3\gamma}}\left(1-\frac{\kappa}{2|a\boldsymbol{K}|^4}\right) \tag{7}$$

$$t_\perp \approx t_0\frac{\kappa}{2|a\boldsymbol{K}|^2\sqrt{1+3\gamma}}. \tag{8}$$

This mapping can be used to obtain a TBG model equivalent to a given double-plate model. The green lines in Fig. 2 show the precision of the mapping at large angles. Deviations between the two are attributed to $\mathcal{O}(\kappa^2)$ and particle-hole asymmetry corrections.

We now demonstrate that, as suggested by the above mapping, the structured double plates indeed develop flat bands as the angle $\theta$ is reduced, just like TBG. Figure 3(a) shows the moiré superlattice and normalized band structure of the double plate and corresponding TBG systems, as the

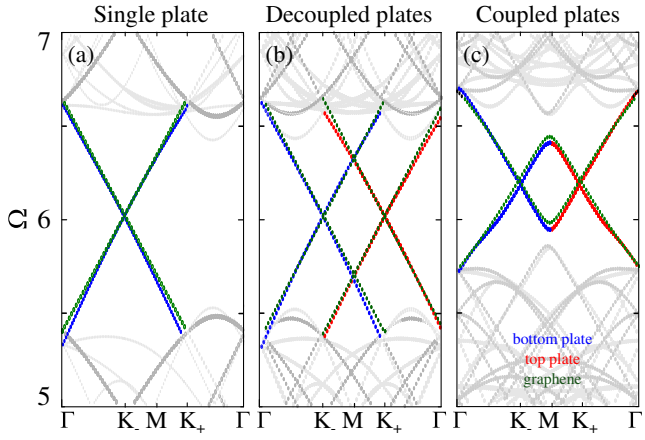


FIG. 2. Band structure of vibrating plates. Dirac cones in the normalized band structure $\Omega(\boldsymbol{k})$ of a single patterned plate (a), two decoupled ($\kappa = 0$) but rotated ($m = 5$, $\theta \approx 6°$) plates (b), and two coupled ($\kappa = 20$) and rotated plates (c). Red and blue denote eigenvalues mostly concentrated on the top and bottom layers, whose respective Dirac points are located at $\boldsymbol{K}_\pm$. The anticrossing at the $M$ point forms a van Hove singularity. In green is the normalized band structure of the equivalent graphene counterparts.

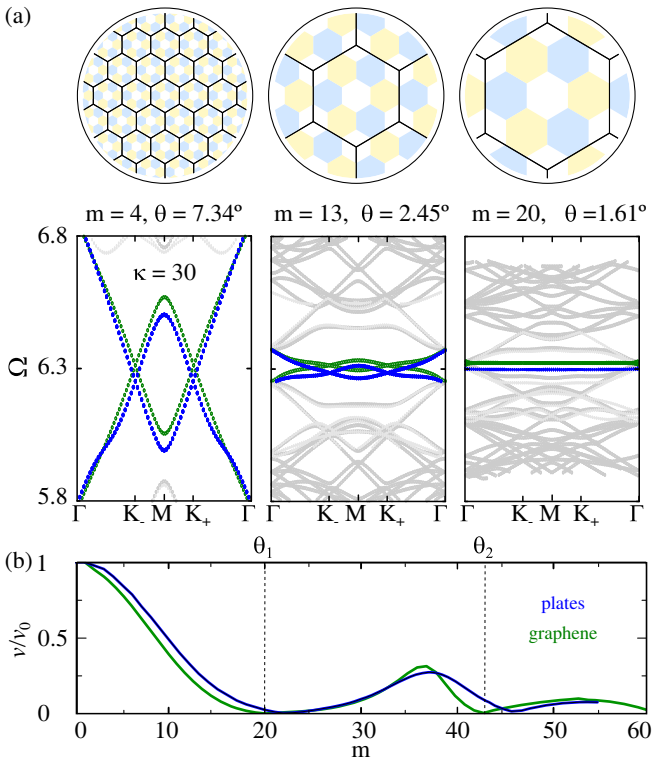


FIG. 3. Flat bands at magic angles in vibrating plates. (a) Flat-band formation as the angle is decreased toward the first magic angle for a double plate system with $\gamma = 2.5$ and $\kappa = 30$ (blue), and the equivalent TBG system (green). (b) Evolution of group velocity $v$ at the Dirac point with twist angle $\theta$, normalized to the Dirac velocity $v_0$ of decoupled layers. The angles with vanishing velocity define so-called magic angles $\theta_n$. For the chosen parameters, $\theta_1 = 1.61°$.

angle $\theta$ decreases from $\theta = 7.34°$ (commensurate index $m = 4$) to $\theta = 1.61°$ ($m = 20$). The latter corresponds approximately to the first magic angle $\theta_1$ for plates with $\kappa = 30$, $\gamma = 2.5$, which corresponds to a TBG with $t_\perp = 0.79$ eV (quite larger than in real TBG, which has $t_\perp \approx 0.48$ eV and a first magic angle at $m \approx 31, \theta \approx 1.05°$.) As $\theta$ approaches $\theta_1$, the $M$-point band anticrossing grows, flattens the Dirac cones, and reduces the Dirac-point group velocity $v(\theta)$. At precisely $\theta = \theta_1$ [rightmost panel in Fig. 3(a)] the Dirac cones collapse into a quasiflat band with exactly zero group velocity. Reducing the angle further leads to repeated reemergences and collapses of the Dirac cones at subsequent, higher-order magic angles $\theta_i$. The corresponding nonmonotonous $v(\theta)$ is shown in Fig. 3(b), both for the double plate (blue) and TBG (green). Both results are very similar, with deviations again attributed to higher-order coupling corrections and particle-hole asymmetries.

We finally compare the spatial profile of the corresponding plate modes to their electron eigenstate counterparts. In magic-angle TBG, the wave function of flat-band electrons is predicted to be algebraically localized around AA for all momenta away from the Γ point [20]. The fact that the states are not exponentially localized is a remarkable feature that highlights the nontrivial chirality-driven nature of the flat-band mechanism in this system. In Fig. 4, we compare the spatial profile of eigenmodes in twisted double plates and TBG.

At twist angles above the first magic angle, the graphene eigenstates exhibit the first hints of AA-region localization. Fig. 4(a) shows an enlargement of the bands at $\theta = 3.15°$ ($m = 10$) in TBG. On their right, we show a selection of eigenstate top-layer densities summed over sublattices for the wave vectors marked with colored circles. States at the $K$ and $M$ points (yellow and purple dots, respectively) exhibit maxima at the AA regions (center of the hexagonal unit cell). At the Γ point, however, the states have a different character. If we select a single Γ state belonging to the red subband (red dot), it exhibits a minimum at AA. However, in the simplest version of the continuum model used here, Γ-point states are triply degenerate. If we plot the total spatial density from the three states (blue dot), the AA minimum is washed out.

The corresponding behavior of $W_+(\boldsymbol{r})$ in the double-plate system, Fig. 4(b), is very similar. The main difference is a lack of energy symmetry around the Dirac point and, notably, a much richer spatial structure present in the eigenmodes, which, unlike for graphene, is well defined throughout the honeycomb unit cell (not only at tight-binding atomic sites). This results in an intricate fast modulation in the moiré supercell that reveals the chiral character of some states (e.g., red dot). The slow envelope of the different eigenmodes, however, quantitatively replicates their graphene counterparts.

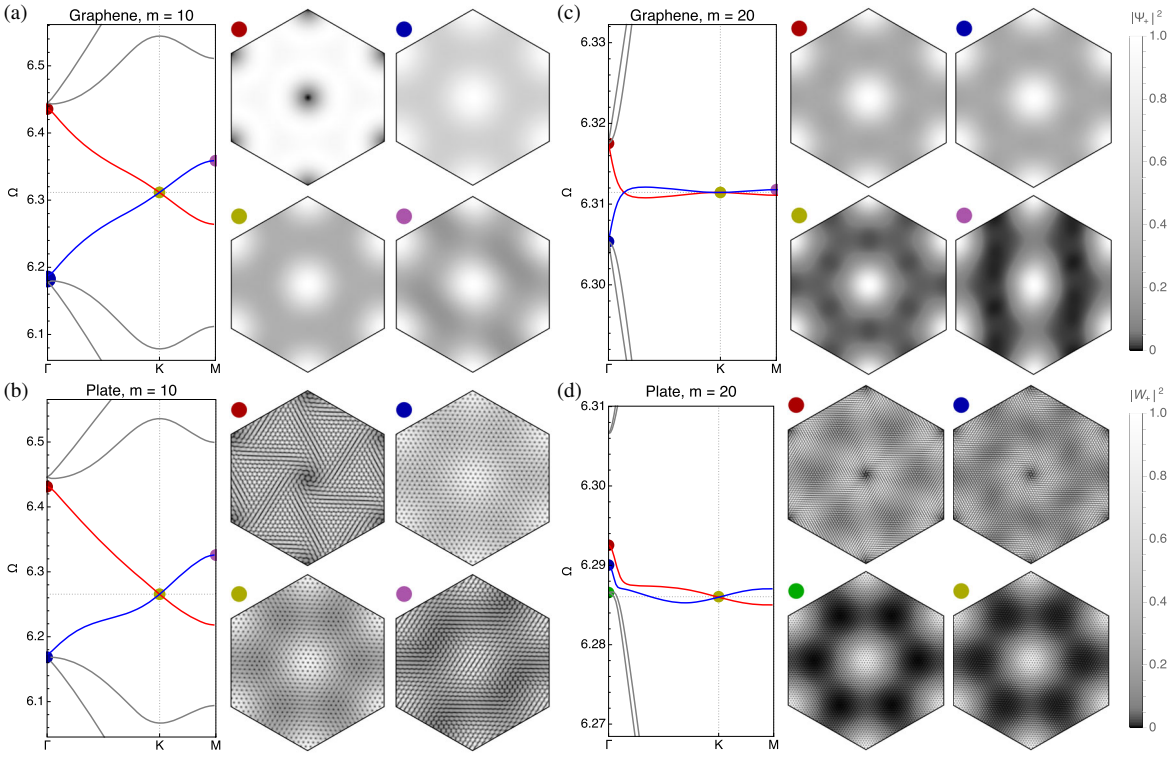


FIG. 4. Low energy (frequency) bands and spatial profile of selected eigenmodes (colored dots) for TBG (a),(c) and the analogous vibrating plate system (b),(d). Twist angles are taken at $m = 10$ (a),(b) and at the first magic angle $m = 20$ (c),(d). Dimensionless parameters are $\kappa = 40$ and $\gamma = 2.5$.

At the first magic angle in graphene ($m = 20$ here), the AA localization within the flat part of the band becomes fully developed [see yellow and purple states in Fig. 4(c)]. Γ states (red and blue) are still far less localized and remain triply degenerate. This is markedly different in the plate system. A true gap opens asymmetrically around the flat band, which no longer connects with higher-frequency bands at Γ. All states away from Γ are again algebraically localized at AA (blue dot). At Γ there are several nondegenerate states close in frequency, exhibiting varying forms of spatial structure, including AA localization (green dot).

*Conclusion.*—Our results demonstrate that the chirality-driven flat-band formation mechanism of TBG can be realized in a classical system of patterned vibrating plates (see Fig. 1). We derived a quantitatively precise mapping between the graphene-based and mechanical systems and demonstrated a very similar modulation of group velocity with twist angles and spatial eigenmode profiles in both. The differences in spectral properties are mostly due to (a) the increased number of spatial degrees of freedom in the plate as compared to the tight-binding graphene models, and (b) the simplified form of the graphene model, which here does not incorporate perturbations that break particle-hole symmetry and Γ-point degeneracies. The exploration of the magic angle sequence and velocity modulation of TBG using the mechanical double-plate analog would allow far easier parameter uniformity and control than in TBG. Mechanical analogs could not only help shed light on the rich TBG physics but would also enable ultrasonic devices for slow-sound operations and rf signal buffering.

F. P. and P. S.-J. acknowledge support from the Spanish Ministry of Science, Innovation and Universities through Grants No. PCI2018-093026 and No. PGC2018-097018-B-I00 (AEI/FEDER, EU). J. C. acknowledges the support from the European Research Council (ERC) through the Starting Grant No. 714577 PHONOMETA and from the MINECO through a Ramón y Cajal grant (Grant No. RYC-2015-17156).

*Note added.*—While this paper was being finalized for publication, a preprint of another work [43] was posted online, with a study of flat bands and magic angles in acoustic analogs of twisted bilayer graphene.

*Corresponding author.
pablo.sanjose@csic.es

[1] W. Zhong and X. Zhang, Phys. Lett. A **375**, 3533 (2011).
[2] D. Torrent, D. Mayou, and J. Sánchez-Dehesa, Phys. Rev. B **87**, 115143 (2013).
[3] C. He, X. Ni, H. Ge, X.-C. Sun, Y.-B. Chen, M.-H. Lu, X.-P. Liu, and Y.-F. Chen, Nat. Phys. **12**, 1124 (2016).
[4] F. Zangeneh-Nejad and R. Fleury, Phys. Rev. Lett. **122**, 014301 (2019).
[5] C.-W. Chen, N. Lera, R. Chaunsali, D. Torrent, J. V. Alvarez, J. Yang, P. San-Jose, and J. Christensen, Adv. Mater. **31**, 1904386 (2019).
[6] P. Gao, D. Torrent, F. Cervera, P. San-Jose, J. Sánchez-Dehesa, and J. Christensen, Phys. Rev. Lett. **123**, 196601 (2019).
[7] R. Chaunsali, E. Kim, A. Thakkar, P. G. Kevrekidis, and J. Yang, Phys. Rev. Lett. **119**, 024301 (2017).
[8] M. Miniaci, R. K. Pal, B. Morvan, and M. Ruzzene, Phys. Rev. X **8**, 031074 (2018).
[9] Y. Chen, X. Liu, and G. Hu, J. Mech. Phys. Solids **122**, 54 (2019).
[10] X. Zhang, M. Xiao, Y. Cheng, M.-H. Lu, and J. Christensen, Commun. Phys. **1**, 97 (2018).
[11] J. M. B. Lopes dos Santos, N. M. R. Peres, and A. H. Castro Neto, Phys. Rev. Lett. **99**, 256802 (2007).
[12] E. Suárez Morell, J. D. Correa, P. Vargas, M. Pacheco, and Z. Barticevic, Phys. Rev. B **82**, 121407(R) (2010).
[13] R. Bistritzer and A. H. MacDonald, Proc. Natl. Acad. Sci. U.S.A. **108**, 12233 (2011).
[14] J. M. B. Lopes dos Santos, N. M. R. Peres, and A. H. Castro Neto, Phys. Rev. B **86**, 155449 (2012).
[15] A. H. Castro Neto, F. Guinea, N. M. R. Peres, K. S. Novoselov, and A. K. Geim, Rev. Mod. Phys. **81**, 109 (2009).
[16] B. Amorim, A. Cortijo, F. de Juan, A. Grushin, F. Guinea, A. Gutiérrez-Rubio, H. Ochoa, V. Parente, R. Roldán, P. San-Jose, J. Schiefele, M. Sturla, and M. Vozmediano, Phys. Rep. **617**, 1 (2016), novel effects of strains in graphene and other two dimensional materials.
[17] A. Luican, G. Li, A. Reina, J. Kong, R. R. Nair, K. S. Novoselov, A. K. Geim, and E. Y. Andrei, Phys. Rev. Lett. **106**, 126802 (2011).
[18] G. Trambly de Laissardière, D. Mayou, and L. Magaud, Phys. Rev. B **86**, 125413 (2012).
[19] P. Moon and M. Koshino, Phys. Rev. B **85**, 195458 (2012).
[20] G. T. de Laissardière, D. Mayou, and L. Magaud, Nano Lett. **10**, 804 (2010).
[21] P. San-Jose, J. González, and F. Guinea, Phys. Rev. Lett. **108**, 216802 (2012).
[22] G. Tarnopolsky, A. J. Kruchkov, and A. Vishwanath, Phys. Rev. Lett. **122**, 106405 (2019).
[23] O. Vafek and K. Yang, Phys. Rev. B **81**, 041401(R) (2010).
[24] H. Isobe, N. F. Q. Yuan, and L. Fu, Phys. Rev. X **8**, 041041 (2018).
[25] D. M. Kennes, J. Lischner, and C. Karrasch, Phys. Rev. B **98**, 241407(R) (2018).
[26] J. González and T. Stauber, Phys. Rev. Lett. **122**, 026801 (2019).
[27] A. O. Sboychakov, A. V. Rozhkov, A. L. Rakhmanov, and F. Nori, Phys. Rev. B **100**, 045111 (2019).
[28] E. Y. Andrei and A. H. MacDonald, arXiv:2008.08129.
[29] Y. Cao, V. Fatemi, A. Demir, S. Fang, S. L. Tomarken, J. Y. Luo, J. D. Sanchez-Yamagishi, K. Watanabe, T. Taniguchi, E. Kaxiras, R. C. Ashoori, and P. Jarillo-Herrero, Nature (London) **556**, 80 (2018).
[30] X. Lu, P. Stepanov, W. Yang, M. Xie, M. A. Aamir, I. Das, C. Urgell, K. Watanabe, T. Taniguchi, G. Zhang, A. Bachtold, A. H. MacDonald, and D. K. Efetov, Nature (London) **574**, 653 (2019).

[31] Y. Cao, V. Fatemi, S. Fang, K. Watanabe, T. Taniguchi, E. Kaxiras, and P. Jarillo-Herrero, Nature (London) **556**, 43 (2018).
[32] C.-C. Liu, L.-D. Zhang, W.-Q. Chen, and F. Yang, Phys. Rev. Lett. **121**, 217001 (2018).
[33] M. Yankowitz, S. Chen, H. Polshyn, Y. Zhang, K. Watanabe, T. Taniguchi, D. Graf, A. F. Young, and C. R. Dean, Science **363**, 1059 (2019).
[34] Y. Cao, D. Chowdhury, D. Rodan-Legrain, O. Rubies-Bigorda, K. Watanabe, T. Taniguchi, T. Senthil, and P. Jarillo-Herrero, Phys. Rev. Lett. **124**, 076801 (2020).
[35] R. Lyu, Z. Tuchfeld, N. Verma, H. Tian, K. Watanabe, T. Taniguchi, C. N. Lau, M. Randeria, and M. Bockrath, arXiv: 2008.06907.
[36] L. A. Gonzalez-Arraga, J. L. Lado, F. Guinea, and P. San-Jose, Phys. Rev. Lett. **119**, 107201 (2017).
[37] A. Thomson, S. Chatterjee, S. Sachdev, and M. S. Scheurer, Phys. Rev. B **98**, 075109 (2018).
[38] A. L. Sharpe, E. J. Fox, A. W. Barnard, J. Finney, K. Watanabe, T. Taniguchi, M. A. Kastner, and D. Goldhaber-Gordon, Science **365**, 605 (2019).
[39] U. Zondiner, A. Rozen, D. Rodan-Legrain, Y. Cao, R. Queiroz, T. Taniguchi, K. Watanabe, Y. Oreg, F. von Oppen, A. Stern, E. Berg, P. Jarillo-Herrero, and S. Ilani, Nature (London) **582**, 203 (2020).
[40] The pure-bending Germain–Lagrange equations neglect internal strain and shear in the plate and are therefore not applicable to atomically thin membranes with $h \to 0$ where these dominate [41].
[41] See Supplemental Material at http://link.aps.org/supplemental/10.1103/PhysRevLett.125.214301 for analytical derivations and results, which includes Ref. [42].
[42] Y. Chen, G. Huang, X. Zhou, G. Hu, and C.-T. Sun, J. Acoust. Soc. Am. **136**, 2926 (2014).
[43] Y. Deng, M. Oudich, N. JRK Gerard, J. Ji, M. Lu, and Y. Jing, companion paper, Phys. Rev. B **102**, 180304 (2020).